A discrepancy analysis methodology for rolling element bearing diagnostics under variable speed conditions

Stephan Schmidt[a,*], P. Stephan Heyns[a], Konstantinos C. Gryllias[b,c]

[a] *Centre for Asset Integrity Management, Department of Mechanical and Aeronautical Engineering, University of Pretoria, Pretoria, South Africa*
[b] *Department of Mechanical Engineering, PMA Division, KU Leuven, Celestijnenlaan 300, 3001 Heverlee, Belgium*
[c] *Dynamics of Mechanical and Mechatronic Systems, Flanders Make, Belgium*

Abstract

Performing condition monitoring on critical machines such as gearboxes is essential to ensure that the machines operate reliably. However, many gearboxes are exposed to variable operating conditions which impede the condition inference task. Rolling element bearing component failures are important causes of gearbox failures and therefore robust bearing diagnostic techniques are required. In this paper, a rolling element bearing diagnostic methodology based on novelty detection is proposed for machines operating under variable speed conditions. The methodology uses the wavelet packet transform, order tracking and a feature modelling approach to generate a diagnostic metric in the form of a discrepancy measure. The probability distribution of the diagnostic metric, statistically conditioned on the corresponding operating conditions is estimated, whereafter the condition of the rolling bearing element is inferred. The rolling element bearing diagnostic methodology is validated on data from a phenomenological gearbox model and two experimental datasets.

Keywords:

Bearing diagnostics, Time variable speed conditions, Novelty detection, Discrepancy analysis, Probabilistic approach

*Corresponding author.
Email address: stephanschmidt@zoho.com (Stephan Schmidt)

1. Introduction

Gearboxes found in air-cooled condenser fans, wind turbines and draglines operate under variable operating conditions, which impede the vibration-based condition monitoring task [1–3]. Lin et al. [4] found that gearbox failures are one of the main causes of wind turbine failures, with rolling element bearing failures being one of the main reasons behind gearbox failures. This emphasises the need for reliable diagnostic techniques that allow incipient rolling element bearing damage to be detected, located (i.e. determine which component is damaged and which damage mode is present) and trended as the bearing deteriorates under varying operating conditions.

A wide variety of techniques have been developed and used for rolling element bearing diagnostics [5], such as envelope analysis which has been extended by [6, 7] for variable speed applications, cyclostationary analysis [8, 9] which can be seen as a generalisation of envelope analysis [8], regression analysis for variable loads [10], empirical mode decomposition and its extensions [11, 12], wavelet analysis [13–16], the spectral kurtosis [17], the kurtogram and its variants [18, 19], the sparsogram [20] and the infogram [21]. Varying rotational speeds complicate the condition monitoring process due to its influence on the properties of the vibration signal [7, 22, 23] and the rotational speed information of the shaft is also required. The rotational speed information can be difficult and impractical to measure for some machines; this makes tacholess order tracking methods very important for condition monitoring under varying speed conditions [24–27]. It can also be quite challenging to infer the condition of the bearing by using wavelet analysis for example. This is because small changes occur in the time-scale distribution of the vibration signal as the bearing deteriorates, which can be difficult to detect. This motivates many researchers to use machine learning techniques to aid with the condition inference task.

Machine learning techniques are extensively used in the condition monitoring field as a data-handling tool which allow inferences to be made from complicated data distributions in multi-dimensional spaces. Artificial neural networks [28], support vector machines [28–30], k-means clustering [31], Gaussian mixture models [32] and hidden Markov models

[14, 32–34] are some examples of the approaches which have been used for bearing diagnostics. However, many of the approaches are based on the assumption that much historical fault data are available for model optimisation, which is rarely achieved in practice. Hence, physics-based models [29] and novelty detection approaches [30, 35–42] have been investigated for the condition inference task when only a physical model of the relationship between the damage modes and the vibration signal or only healthy data are available for feature model optimisation. A few different novelty detection categories can be used as summarised in Ref. [38]. The basic principle of novelty detection is to assign a novelty score to the data with a model only optimised on a healthy dataset. Depending on the novelty score, the label of the data is either normal or a novelty. Support vector machines and related techniques [30, 41, 43], self-organising maps [40], hidden Markov models [34] and Gaussian models [42] are some examples of models used for bearing novelty detection. In the paper by Timusk et al. [39], many novelty detection techniques are compared for gearbox and motor novelty detection and it was found that a combination classifier algorithm performs the best for novelty detection of transient signals. Georgoulas et al. [44] found that a majority voting anomaly detection scheme improves the novelty detection capabilities of individual models for bearing fault detection.

Discrepancy analysis is a novelty detection approach which has been successfully used for gear diagnostics under varying operating conditions [36, 37, 45, 46] and is investigated for rolling element bearing diagnostics under variable speed conditions in this paper. In discrepancy analysis, localised discrepancy measures are obtained for the dataset under consideration using a model of the healthy data. The localised discrepancy measure is a novelty detection score that quantifies the deviation of the segment under consideration from the feature model of the healthy data and can be obtained from Gaussian models, Gaussian mixture models [37], neural networks [36] and hidden Markov models [46]. The discrepancy measure is used to form a discrepancy signal which is processed so that the condition of the component can be inferred. The difference between discrepancy analysis and other novelty detection techniques is that a localised novelty score is given as opposed

to a novelty score for the whole measurement. The generated discrepancy signal can be processed into more useful information which allows not only a novelty to be detected, but the characteristics of the novelty i.e. the damaged component can be inferred as well [46].

The new contributions of the current work can be summarised as:

- A framework for rolling element bearing diagnostics is developed using discrepancy analysis for machines operating under varying speed conditions. This methodology allows for the detection, the localisation and trending of bearing faults.

- Discrepancy signal processing tools are investigated and proposed to assist with the condition inference task. An estimate of the conditional model of the discrepancy measure given the rotational speed is used to mitigate the adverse influences of the varying speed conditions.

The objective of the proposed methodology is not to replace classical bearing diagnostic techniques such as wavelet analysis or envelope analysis, but rather to develop a novelty detection framework into which the aforementioned techniques can be naturally incorporated.

The layout of the paper is as follows: The methodology is firstly presented in Section 2. Moreover it is validated on phenomenological gearbox model data in Section 3 and on experimental data in Section 4, respectively. Furthermore, conclusions and recommendations are made in Section 5. For the sake of completeness, additional information concerning the discrepancy processing technique, presented in Section 2.5, has been added in Appendix A. Finally in Appendix B the parameters of the phenomenological gearbox model, presented in Section 3, can be found.

2. Diagnostic methodology

2.1. Overview

The general process diagram for discrepancy analysis is presented in Figure 1. The ex-

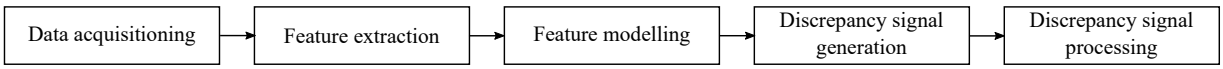

Figure 1: The key steps in the rolling element bearing diagnostic methodology.

act discrepancy analysis procedure implemented in this paper is presented in Figure 2 and is used throughout this work. However, one of the benefits of the proposed methodology is that sub-processes such as the feature extraction procedure can be replaced with a more appropriate procedure if desired. Vibration measurements are used as source of condition

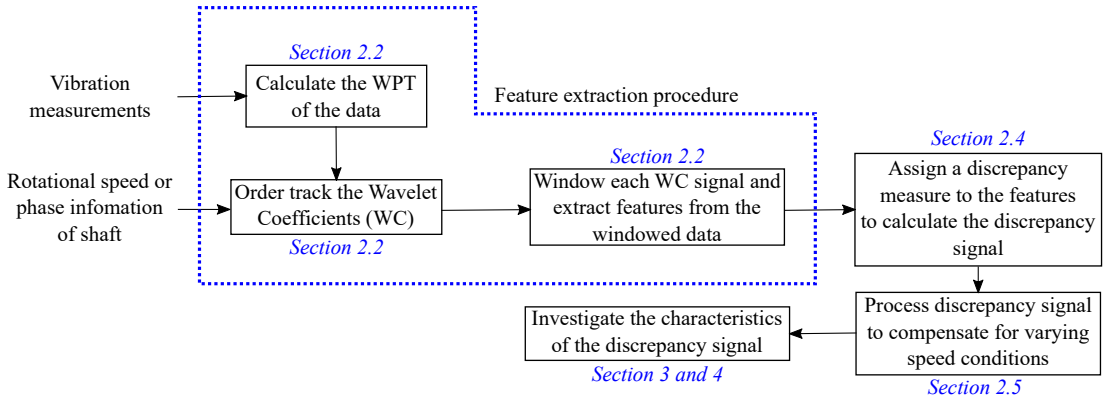

Figure 2: The steps in the methodology used in subsequent investigations are presented. It is assumed that the model parameters used to generate the discrepancy signal are already estimated with the method in Section 2.3 and therefore this step is excluded from the process diagram. Different characteristics of the discrepancy signal are investigated for the different datasets and therefore only Section 3 and Section 4 are referenced in this figure, with the relevant information included in those sections as well. Abbreviations: Wavelet Packet Transform (WPT), Wavelet Coefficients (WC).

monitoring data, because the measurements are easy to obtain, non-intrusive in nature and rich with diagnostic information pertaining to the machine to which the transducers are connected. In the training phase, the features are extracted from the healthy vibration data, whereafter the features are modelled with a statistical model. In the testing phase, the features are extracted with the same approach as in the training phase, but the model of the healthy features are used to generate a discrepancy measure. The sequence of consecutive discrepancy measures is used to form a discrepancy signal which is processed to infer the presence of bearing damage.

2.2. Feature extraction

The feature extraction process that is used in this paper, is presented in Figure 3. Wavelet analysis is used in the feature extraction process, because it proved successful

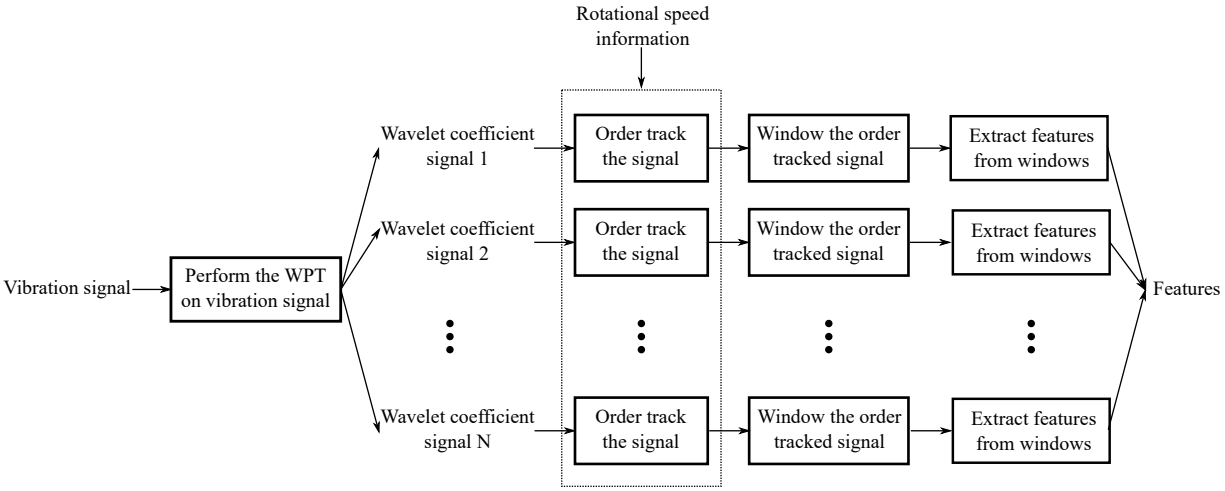

Figure 3: The feature generation process used in the proposed methodology. The features are in the angular domain due to the order tracking that is performed in the process. The abbreviations are, WPT: Wavelet Packet Transform; N: Total number of wavelet coefficient signals.

in detecting singularities and it is sensitive to impulses induced by bearing damage [47]. The Wavelet Packet Transform (WPT) is used in this paper because it has the benefit that the exact characteristic frequencies do not have to be known a priori (as opposed to the continuous wavelet transform where the exact frequencies such as the resonance frequencies have to be specified) and the high frequency bands have a high resolution as well (as opposed to the discrete wavelet transform). The WPT decomposes the signal into a set of wavelet coefficients with a filter bank of scaling and wavelet basis functions, where the wavelet coefficients are associated with specific sub-bands. The wavelet coefficients are dependent on the wavelet basis function, the appropriate choice depending on the characteristic that needs to be detected, and the level of decomposition, which depends on the frequency resolution that is required for the wavelet coefficients. The WPT is applied to the time domain signal, because the resonances which are excited by the bearing damage are independent of the rotational speed.

The features need to be sensitive to the presence of impulses, which manifest as time-localised bursts of energy and are quasi-periodic with respect to shaft angle due to rolling

element slip. Hence, the extracted wavelet packet coefficients are subsequently order tracked with rotational speed information to transform it from the time to the angle domain. Hence, the order tracked wavelet coefficients preserve the angle-time cyclostationary properties of the bearing damage [22, 23]. Rotational speed or phase information can be obtained from optical probes and shaft encoders [48] or in the absence of the rotational speed measurement equipment, tacholess order tracking approaches can be used [24–27]. Only computed order tracking methods are used in this paper, due to the availability of the rotational speed information. In the feature extraction procedure of discrepancy analysis, the angular information of the original vibration signal needs to be retained and therefore localised features are extracted from the order tracked wavelet coefficients. This is performed by windowing the wavelet coefficients with rectangular windows whereafter the Root-Mean-Square (RMS) is extracted from the windows as features. The RMS of the windowed wavelet coefficient is appropriate as a feature, because the localised energy and not the frequency characteristics of the windowed data are important. The windowing procedure is illustrated in Figure 4 for a single wavelet coefficient signal extracted by applying the WPT on a synthetic bearing signal immersed in noise. The RMS of the windowed wavelet coefficients improves the sensitivity of the wavelet coefficients to damage and is therefore ideal for discrepancy analysis. The windows do not overlap in Figure 4 to make the illustration easier to understand. In the methodology, rectangular windows as opposed to Hamming windows for example are used to ensure that no information is lost and overlapping windows are used to ensure that no information on the edges of the non-overlapping windows is lost. The number of windows per shaft revolution should be more than twice the fault order that needs to be detected, but the window length should be sufficiently long to ensure that the statistics are properly estimated. It is suggested that the overlap should at least be 50% between coinciding windows to ensure that no information on the edges are lost.

Using additional statistics such as the kurtosis can potentially improve the diagnostic capabilities of discrepancy analysis, especially for incipient damage detection. However,

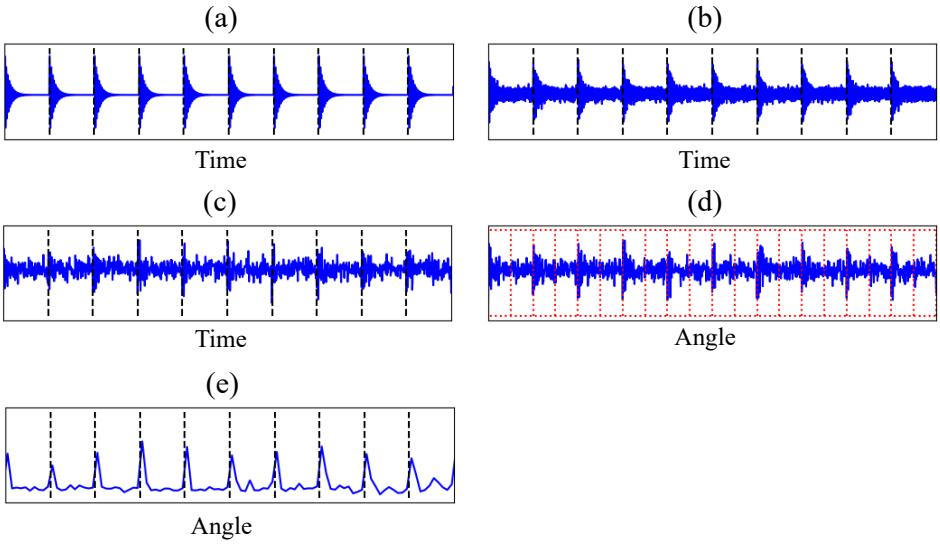

Figure 4: The windowing procedure is illustrated for a synthetic signal under constant operating conditions. In (a), a train of bearing impulses is shown. In (b), broadband Gaussian noise is added to the signal in (a) and is used for subsequent analyses. The WPT with a decomposition level of N_{dec} is performed on the signal in (b) which resulted in $2^{N_{dec}}$ wavelet coefficient signals. In (c), a single wavelet coefficient signal is shown and windowed with 20 non-overlapping windows in (d). The signal in (c) is order tracked to obtain the signal in (d). Finally, the RMS is extracted from the windows in (d) and a signal with 20 samples is shown in (e). The procedure in (d) and (e) is repeated for all $2^{N_{dec}}$ wavelet coefficients to obtain $2^{N_{dec}}$ signals similar to (e) which constitute the 2^{dec}-dimensional feature set which consist of 20 observations.

optimising the discrepancy analysis procedure is beyond the scope of this work. The magnitude of the bearing impulses and of the vibration signal are dependent on the operating conditions, which can cause problems when performing condition inference. This aspect is addressed in Section 2.5.

The window length is selected as $2\pi/20$ rad with a 50% overlap, to allow localised impulses to be detected. Wu and Liu [49] found that the Daubechies db20 wavelet basis function outperformed the Daubechies db4 and db10 wavelet basis functions for engine diagnostics and the Daubechies db20 has the shape of an impulse, which is why it is used in this paper. The level of the decomposition, denoted by N_{dec}, is related to the number of wavelet coefficients by $2^{N_{dec}}$, with only the wavelet coefficients of the final decomposition level used for feature extraction. Hence, as only the RMS of the windowed wavelet coefficients is calculated and there are $2^{N_{dec}}$ wavelet coefficients, the dimensionality of the feature space (i.e. the number of features) is equal to $D = 2^{N_{dec}}$. The level of the

decomposition is $N_{dec} = 4$ for all datasets investigated in this paper which result in 16 wavelet coefficients. This means that the dimensionality of the feature space is 16, which provides an ideal compromise between having sufficient resolution to detect changes in localised spectral frequency bands but also to have a sufficiently low dimensionality to avoid the curse of dimensionality.

It should be noted that an optimisation process cannot be performed in order to select the most appropriate wavelet basis function and the best decomposition level for bearing diagnostics, as only healthy data are available. Dimensionality reduction techniques, such as principal component analysis [50], can also be performed to alleviate the problems associated with the curse of dimensionality, but is not performed in this investigation due to the relatively low dimensionality of the feature space and the models that are used. The features used in this paper are not necessarily optimal for bearing diagnostics and features from cyclostationary analysis techniques such as the instantaneous power spectrum and from the empirical mode decomposition can also be investigated in future analyses.

2.3. Feature modelling

The features, extracted in Section 2.2 from the healthy data, can be modelled with a Gaussian model, a Gaussian mixture model or a hidden Markov model to list a few examples. In this paper, a Gaussian model is used to model the features extracted from the healthy data. The motivation for using a Gaussian model as opposed to other models is that it is very simple to implement and with the post-processing, which will be presented in Section 2.5, it is robust to varying speed conditions.

The D-dimensional features extracted from window i are denoted by $\boldsymbol{b}_i \in \mathbb{R}^{D\times 1}$, with the features of the healthy machine denoted by $\boldsymbol{b}_i^{train} \in \mathbb{R}^{D\times 1}$. The training feature set $\{\boldsymbol{b}_i^{train}\}$ comprises of N_{obs} observations of the D-dimensional features and is used to obtain the parameters of the model. The maximum likelihood estimates of the mean $\boldsymbol{\mu_b} \in \mathbb{R}^{D\times 1}$

and the covariance $\boldsymbol{\Sigma_b} \in \mathbb{R}^{D\times D}$ of the healthy feature set $\{\boldsymbol{b}_i^{train}\}$ are given by [50]

$$\boldsymbol{\mu_b} = \frac{1}{N_{obs}} \sum_{i=1}^{N_{obs}} \boldsymbol{b}_i^{train}, \tag{1}$$

$$\boldsymbol{\Sigma_b} = \frac{1}{N_{obs}} \sum_{i=1}^{N_{obs}} (\boldsymbol{b}_i^{train} - \boldsymbol{\mu_b})(\boldsymbol{b}_i^{train} - \boldsymbol{\mu_b})^T, \tag{2}$$

where the transpose is denoted by superscript T. If a single measurement is used to obtain the model parameters, N_{obs} is equal to the number of windows used for extracting features from the measurement. If multiple measurements are used to obtain the model parameters, then the extracted features of the respective measurements are concatenated together to form a single D-dimensional training set with a total of N_{obs} samples.

2.4. Discrepancy signal generation

The Mahalanobis distance is used as the discrepancy measure, which quantifies the deviation of the new data point from the model of the healthy data. The discrepancy measure is denoted by η_j for the features associated with the window j [50]

$$\eta_j = \sqrt{(\boldsymbol{b}_j - \boldsymbol{\mu_b})^T \boldsymbol{\Sigma_b}^{-1} (\boldsymbol{b}_j - \boldsymbol{\mu_b})}, \tag{3}$$

where the model parameters are obtained using Equations (1) and (2) from the healthy data, and $\boldsymbol{b}_j$ denotes the features, extracted from the wavelet coefficients in the jth window, of the testing feature set. The Mahalanobis distance is proportional to the negative logarithm of the probability density function of a Gaussian model, where the latter is in general available for all probabilistic models. The discrepancy measure, obtained from each time step, is used to form a discrepancy signal which can be processed to develop a diagnostic metric so that the condition of the bearing can be inferred. Therefore, the discrepancy signal $\boldsymbol{\eta} \in \mathbb{R}^{N_{obs}\times 1}$ corresponds to the features extracted from the N_{obs} windows applied to the vibration measurement under consideration.

2.5. Processing the diagnostic metric

The discrepancy signal is obtained in terms of shaft angle or shaft revolutions and need to be processed and analysed so that the condition of the bearing can be inferred. The simplest processing technique is to calculate the RMS of the discrepancy signal, but it will only be possible to detect and trend damage and it will not be possible to perform fault localisation. Even though the discrepancy signal is relatively robust to varying operating conditions, it is not immune to it. Due to the sensitivity of the transmission path, between the excitation source and the measurement point, to the rotational speed and the presence of resonances, it is expected that the discrepancy measure η will be dependent on the rotational speed ω.

Bartelmus and Zimroz [2] and Zimroz et al. [10] showed that the parameters of a linear regression model, aiming to capture the relationship between the diagnostic metric and the operating conditions, are very good condition monitoring metrics. In this paper, the conditional distribution $p(\eta|\omega)$ is modelled and used to mitigate the adverse influences of the varying speed conditions on the diagnostic metric. It is possible to model $p(\eta|\omega)$ by using Bayesian linear regression for example, however standard regression approaches assume that the noise has constant statistical properties [50], which is not always true for the data considered. In Figure 5, the sensitivity of the discrepancy measure with respect to rotational speed is presented for a phenomenological gearbox model, discussed in Section 3, that contains no bearing damage. The mean as well as the variance of the discrepancy measure conditioned on the rotational speed are dependent on the rotational speed, with a resonance band being excited approximately at 105 rad/s. The data, presented in Figure 5, are introduced in this section to motivate and illustrate the processing method that is used in this paper.

Heteroscedastic models are a class of models where the noise in the data is assumed to be a function of the inputs [50–52]. Mixture density networks [50], Gaussian processes [51] and Bayesian neural networks [52] have been used and extended for heteroscedastic models. The computational complexity of the aforementioned regression models increase

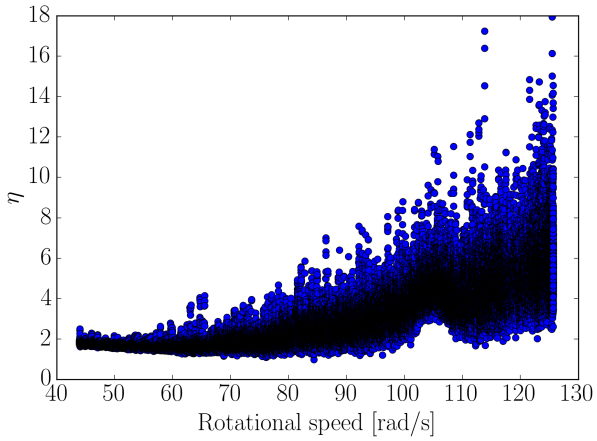

Figure 5: The discrepancy measure η vs. the rotational speed ω from the phenomenological gearbox model, considered in Section 3.

because Monte Carlo Markov Chain (MCMC) [51] or gradient-based optimisation methods are required [52] to estimate the noise parameters.

In this paper, a very simplified non-parametric model is used to estimate the conditional distribution $p(\eta|\omega)$. If the assumption is made that the statistics of the discrepancy measure are independent of the input for small changes in the rotational speed, and that a sufficient amount of training data is available, then the conditional mean

$$\mu_{\eta|\omega}(\omega) = \mathrm{LI}\left(\{\Omega_i\}, \{\mu_{\Omega_i,\Delta\Omega}\}, \omega\right), \tag{4}$$

and variance

$$\sigma^2_{\eta|\omega}(\omega) = \mathrm{LI}\left(\{\Omega_i\}, \{\sigma^2_{\Omega_i,\Delta\Omega}\}, \omega\right), \tag{5}$$

can be good approximations for the actual conditional mean and variance for a specific rotational speed ω. The approach uses the discrepancy measures of the training dataset which correspond to a specific operating condition range $\omega \in \left[\Omega_i - \frac{1}{2}\Delta\Omega,\ \Omega_i + \frac{1}{2}\Delta\Omega\right]$ to calculate the mean $\mu_{\Omega_i,\Delta\Omega}$ and the variance $\sigma^2_{\Omega_i,\Delta\Omega}$. A set of window centres $\{\Omega_i\}$ are generated with a preselected window length $\Delta\Omega$ to generate a corresponding set of localised means $\{\mu_{\Omega_i,\Delta\Omega}\}$ and variances $\{\sigma^2_{\Omega_i,\Delta\Omega}\}$ of the discrepancy measure η; whereafter the linear interpolation function, denoted by LI, is used to predict the conditional mean

$\mu_{\eta|\omega}$ given the rotational speed ω with Equation (4). An overview of the procedure that was used to arrive at Equation (4) and Equation (5) is given in Appendix A.

The benefits of this conditional modelling approach, as opposed to Bayesian regression for example, is that

- no a priori assumptions are made about the form of $\mu_{\eta|\omega}(\omega)$ nor $\sigma^2_{\eta|\omega}(\omega)$,
- it can be extended to other noise distributions,
- it is very computationally efficient as opposed to models requiring MCMC simulations, which is an advantage when performing condition monitoring.

The quality of the fit, using Equation (4) and Equation (5), depends on the distance between the window centres $\{\Omega_i\}$ and the window length $\Delta\Omega$. The unknown window length $\Delta\Omega$ is selected with a grid search optimisation process in this paper. A grid of candidate window lengths is generated and then the following process is followed for each candidate window length on the grid and a preselected window overlap:

1. Calculate the set of window centres $\{\Omega_i\}$, the conditional mean $\{\mu_{\Omega_i,\Delta\Omega}\}$ and the variance $\{\sigma^2_{\Omega_i,\Delta\Omega}\}$ based on the current window length and the window overlap. The position of the window centre k is determined from

$$\Omega_k = \frac{1}{2}\Delta\Omega + k\left(\Delta\Omega - \Omega_{overlap}\right), \tag{6}$$

   for $k = 0, 1, \ldots$, where the window overlap is denoted by $\Omega_{overlap}$ and the window overlap fraction is given by $\Omega_{overlap}/\Delta\Omega$.
2. Discretize the rotational speed axis with a fixed resolution $\Delta\omega$, by starting at the minimum rotational speed ω_{min}. This discretization process is used in the next step to evaluate the suitability of the current window length. A relatively fine resolution of $\Delta\omega = 0.1$ rad/s is used for all future investigations in this paper.

3. Evaluate the following cost function

$$C = \sum_{k=1}^{N-1} \left(\mu_{\eta|\omega}(\omega_{min} + k\Delta\omega) - \mu_{\eta|\omega}(\omega_{min} + (k-1)\Delta\omega) \right)^2, \tag{7}$$

where N is the number of grid-points that were generated in the previous step. The function in Equation (7) gives an indication on how smooth $\mu_{\eta|\omega}(\omega)$ is.

4. Change the window length $\Delta\Omega$ and then repeat the process until all grid points are evaluated.

The cost function in Equation (7) was evaluated for the data presented in Figure 5 for a grid of window lengths and three window overlap fractions i.e. $\Omega_{overlap}/\Delta\Omega$. The window length which is selected from the process, is indicated by the ideal label in Figure 6 and is not the window length that corresponds to the smallest value of the cost function. If the window length is too long, $\mu_{\eta|\omega}(\omega)$ will be too smooth to capture the localised trend within the data. This is presented in Figure 7, where the results of different window

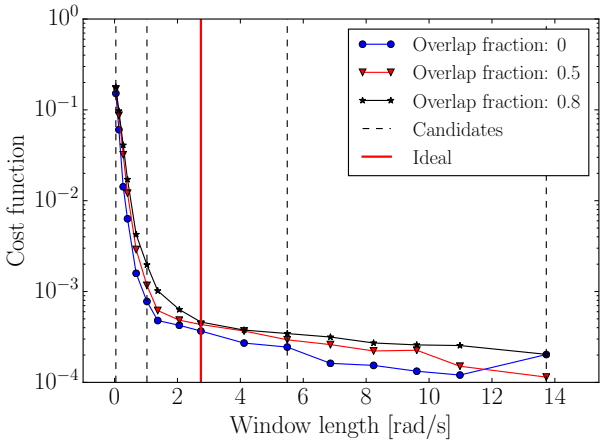

Figure 6: The cost function in Equation (7) is evaluated for several window lengths, with the vertical candidate lines indicating the window lengths which are investigated in subsequent figures. The overlap fraction is obtained by $\Omega_{overlap}/\Delta\Omega$.

lengths (indicated by the candidate lines in Figure 6) are presented for the data shown in Figure 5. All of the curves $\mu_{\eta|\omega}(\omega)$ for the different window lengths $\Delta\Omega$ are shown over one another in Figure 7(i). In Figure 7(ii), each curve is given a different offset which helps to compare the different results that are obtained. It is concluded from the results that all

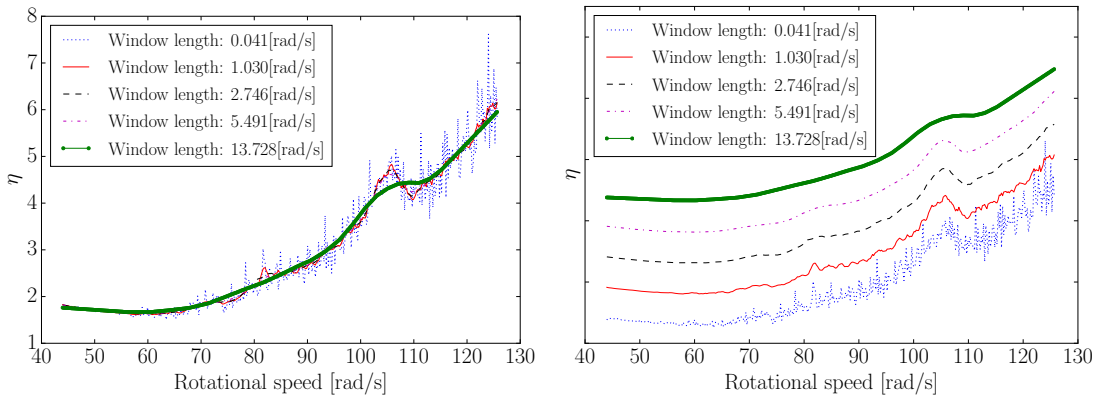

Figure 7: Two plots of the function $\mu_{\eta|\omega}$ are shown for the candidate lines and the ideal line in Figure 6. In Figure 7(i) the fitted function is shown on the actual ordinate, and in Figure 7(ii) a unique value is added to η for each dataset to separate the fitted functions for a simpler visual interpretation. An overlap fraction of 0.8 is used.

curves have the same trend, however if the window length is too small a very noisy function is obtained while a too large window length results in an overly smooth curve which does not fully capture the local characteristics of the data. A window length between 1.5 rad/s and 5.5 rad/s gives sufficiently good results for the data under consideration. The window fraction overlap of 0.8 was used for all investigations, because it provides smoother results without losing local information.

Equation (4) and Equation (5) are ultimately used to scale the discrepancy measure for the features associated with window j of the testing set, denoted by η_j, with

$$\xi_j = \frac{\eta_j - \mu_{\eta|\omega}(\omega_j)}{\sigma_{\eta|\omega}(\omega_j)} \tag{8}$$

where ξ_j denotes the new, scaled discrepancy measure and ω_j denotes the average rotational speed for the features associated with window j. The above procedure can be extended to other distributions, for example if the actual distribution $p(\eta|\omega)$ is skew in the direction where the discrepancy measure increases, the logarithm of the discrepancy measure $\log \eta$ can be used instead of η to make the distribution more symmetric. The benefits of the proposed discrepancy processing procedure, proposed in this section, are only seen when applied under time varying speed conditions and will not be seen under

constant operating conditions.

The proposed methodology as presented in Figure 2 is investigated on phenomenological gearbox model data in the next section, whereafter it is investigated on experimental data in Section 4.

3. Numerical validation

3.1. Phenomenological model

The phenomenological gearbox model that is used in this paper, is from the paper by Abboud et al. [7]. The model developed by Abboud et al. [7] approximates complicated physical phenomena such as other damaged machine components and the sensitivity of the signal's amplitude to varying rotational speeds, while it is simple to implement and computationally efficient to calculate, as opposed to lumped-mass and finite element gearbox models aiming to replicate the same phenomena. The casing or measured vibration signal for the gearbox is decomposed into four distinct parts [7]

$$x_c(t) = x_{dg}(t) + x_{rg}(t) + x_b(t) + x_n(t), \tag{9}$$

where the deterministic gear component x_{dg}, the random gear component x_{rg}, the bearing component from a defective bearing x_b and the noise x_n components can be decomposed into the signal at the source, convoluted with the associated impulse response function to the point of measurement [7]. The decomposition of the signals

$$x_{dg}(t) = h_{dg} \otimes q_{dg}(t), \tag{10}$$

$$x_{rg}(t) = h_{rg} \otimes q_{dg}(t), \tag{11}$$

$$x_b(t) = h_b \otimes q_b(t), \tag{12}$$

is written in terms of the impulse response function h_i, the signal at the source q_i and the convolution operator is denoted by $\otimes$. The impulse response function is written as a

single degree of freedom system with viscous damping

$$h_i(t) = e^{-\zeta_i 2\pi f_{n,i} t} \sin\left(2\pi\sqrt{1-\zeta_i^2} f_{n,i} t\right), \tag{13}$$

where the damping ratio of component i is denoted by ζ_i and the natural frequency of component i is denoted by $f_{n,i}$. The deterministic gear component at the source, simulates the excitation due to the gear mesh excitation

$$q_{dg}(t) = M_{dg}(\omega_r(t)) \sum_{k=1}^{N_{dg}} A_{dg}^{(k)} \cos\left(kN_{t,g} \int_0^t \omega_r(\tau) d\tau + \varphi_{dg}^{(k)}\right), \tag{14}$$

where N_{dg} is the number of gear mesh components which are considered, $A_{dg}^{(k)}$ is the amplitude of the kth component, $\varphi_{dg}^{(k)}$ is the phase of the kth component, $\omega_r(t)$ is the rotational speed of the shaft in radians per second and $N_{t,g}$ is the number of teeth on the gear that is connected to the shaft under consideration. The monotonic function $M_{dg}(\omega_r)$, simulates the dependence of the amplitude of the signal component on the rotational speed. The random gear component, simulates distributed gear damage, and is incorporated to complicate the bearing condition inference task

$$q_{rg}(t) = M_{rg}(\omega_r(t)) \varepsilon_{rg}(t) \sum_{k=1}^{N_{rg}} A_{rg}^{(k)} \cos\left(k \int_0^t \omega_r(\tau) d\tau + \varphi_{rg}^{(k)}\right), \tag{15}$$

and it incorporates similar components as Equation (14), except for a random component ε_{rg}, obtained from

$$\varepsilon_{rg}(t) \sim \mathcal{N}(0, \sigma_{rg}^2), \tag{16}$$

where $\mathcal{N}(0, \sigma_{rg}^2)$ is a zero-mean Gaussian distribution with variance σ_{rg}^2 and $\sim$ denotes that a random sample is taken from the distribution. The noise from other components such as ambient effects is written as

$$x_n(t) = \varepsilon_n(t) M_n(\omega_r(t)), \tag{17}$$

where the monotonic function of ω_r is denoted by M_n and the random component

$$\varepsilon_n(t) \sim \mathcal{N}(0, \sigma_n^2), \tag{18}$$

is a sample from a zero-mean Gaussian function with constant variance σ_n^2.

Lastly, the damaged bearing signal is addressed. The outer race damage is simulated as a train of Dirac functions

$$q_b(t) = F_{dam} \cdot F_{const} \cdot M_b(t) \sum_{i=1}^{N_\mathcal{T}} \delta(t - \mathcal{T}_i), \tag{19}$$

centred at $\mathcal{T}_i$, where $\mathcal{T}_i$ depends on the characteristics of the bearing, slip in the bearing as well as the shaft speed. Hence, the angle of the impacts with respect to shaft orders, is calculated in the angle domain and transformed back to the time domain using the relationship between shaft angle and time. The bearing slip is introduced by adding zero mean Gaussian noise with a standard deviation of 0.1 to the expected impact angles. The constant F_{const} is independent of the fault severity and F_{dam} is proportional to the bearing impulse magnitude. The bearing component F_{dam} is in the form of $F_{dam} \sim \mathcal{N}(\bar{F}_{dam}, \sigma^2_{F_{dam}})$, which simulates the fact that the magnitudes of the bearing impulses are not constant. By changing $\bar{F}_{dam}$, the magnitude of the impulse increases but it does not necessarily mean that the crack size or damage size increases with the same proportion. El-Thalji and Jantunen [53] gave a very good pictorial overview of the evolution of a damaged bearing response. Only changes in $\bar{F}_{dam}$ is investigated in this paper, with $q_b(t) = 0$ being used to simulate a healthy bearing.

3.2. Characteristics of the model

The model characteristics which are used in the equations of the model, are provided in Appendix B. The Ballpass Frequency for the Outer race (BPFO) damage or the characteristic frequency of 2.57 shaft orders is used in this section.

3.3. Vibration data

The proposed methodology is investigated on the phenomenological gearbox model presented in Section 3.1 with the characteristics discussed in Section 3.2. The four rotational speed profiles, investigated for this model

$$\omega_{r,1}(t) = 2\pi(1.3t + 7), \tag{20}$$

$$\omega_{r,2}(t) = 2\pi(5\sin(0.4\pi t) - 20\,(0.1t - 0.5)^2 + 15), \tag{21}$$

$$\omega_{r,3}(t) = 2\pi(6.5\cos(0.2\pi t) + 13.5), \tag{22}$$

$$\omega_{r,4}(t) = 2\pi(6.5\sin(0.2\pi t) + 13.5), \tag{23}$$

and given in rad/s, are shown in Figure 8. The four operating conditions were selected to have the same maximum and minimum values and the same mean. Only the healthy

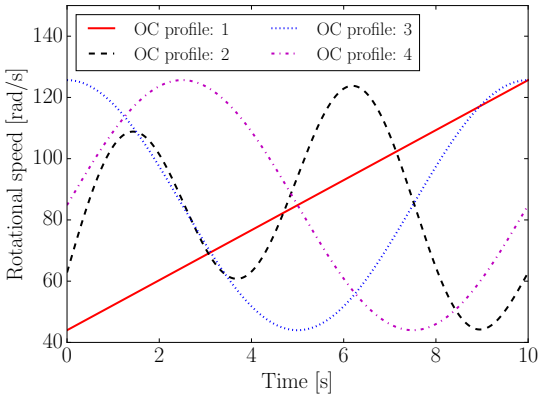

Figure 8: The four rotational speed profiles $\omega_{r,i}$ for the phenomenological model are presented, where the i in $\omega_{r,i}$ denotes the operating condition profile number indicated in the Figure. The corresponding equations of rotational speed profiles are given in Equation (20) to Equation (23).

data for the first three operating conditions are used for the model optimisation process. The casing vibration signal and the corresponding spectrogram for the second operating condition profile are presented in Figure 9 for a fault severity $\bar{F}_{dam} = 1$. The meshing components, the resonance band excited by the gear meshing components at 2.0 kHz as well as the resonance band excited by the random gear component at 3.5 kHz are clearly seen in the spectrogram presented in Figure 9(ii). However, the resonance band that is excited by the bearing impulses at 5.0 kHz is not seen in the spectrogram. The ability of

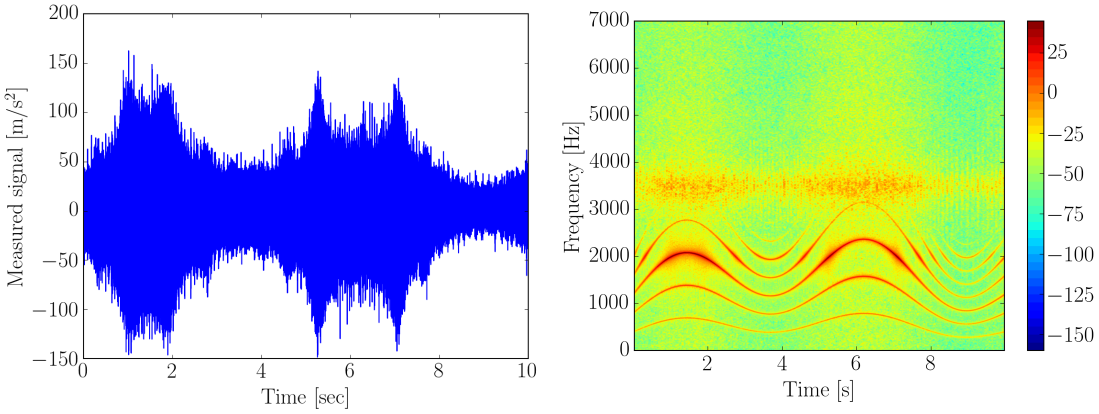

(i) (ii)

Figure 9: The casing vibration signal is shown in its time and the time-frequency domain representations for the second operating condition profile in Figure 9(i) and Figure 9(ii), respectively.

the methodology to detect the presence of damage in the signal model is investigated in the next section.

3.4. Results

The feature extraction procedure in Section 2.2 and the feature modelling procedure in Section 2.3 were applied to the healthy vibration data of the first three operating condition profiles. The discrepancy measure, generated using Equation (3), is firstly obtained for the healthy data and is presented with the corresponding rotational speed in Figure 5. Features are extracted from the order tracked and windowed wavelet coefficients after which a discrepancy measure is obtained for the 16 features extracted from each window. The discrepancy measure, denoted by η, is processed with Welch's power spectral density to calculate how its energy is distributed in the frequency domain with unit orders instead of Hertz. The spectrum in Figure 10 is presented for the four operating conditions that are under consideration as well as for three fault severities (FS) where $\bar{F}_{dam}$, used in Equation (19), is equal to 1, 2 and 4, respectively.

The BPFO frequency components in shaft orders are detected in all three cases, and as the damage increases the amplitude of the BPFO and its harmonics increase as well. However, the amplitude of the BPFO is different for the various operating conditions given the same fault severity. As a result, it is difficult to distinguish between changes in

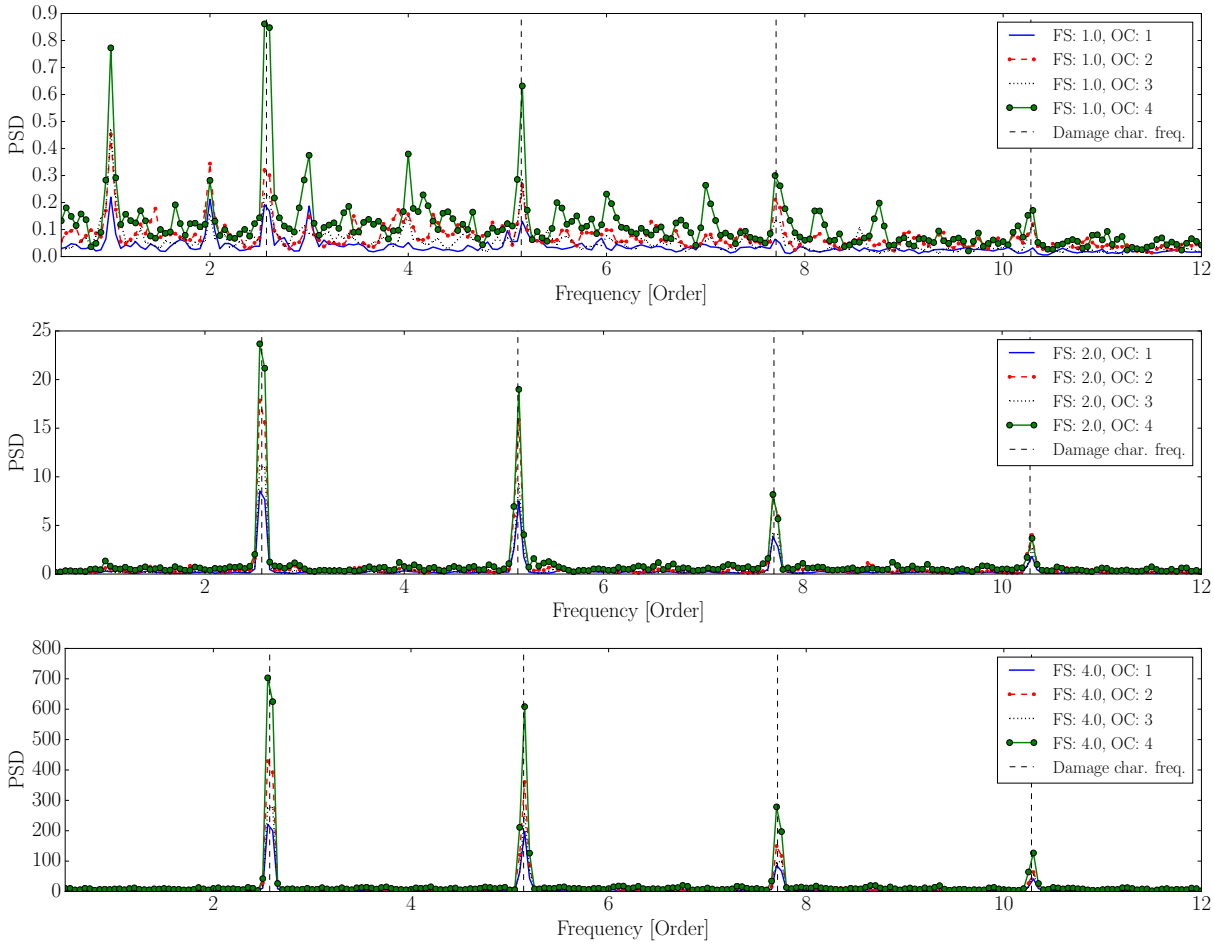

Figure 10: Comparing the spectrum of the discrepancy signals for the four operating conditions and the three fault severities (FS) which are investigated. The fault severity value indicates the value of $\bar{F}_{dam}$ that is used. Note that different scales are used for the three cases.

operating condition and changes in machine condition.

However, to make the results more robust, it is necessary to take into account the fact that the vibration signal and its components are dependent on the operating conditions. The conditional modelling procedure in Section 2.5 is used to obtain the conditional statistics. Equation (4) is used to obtain $\mu_{\eta|\omega}$ and Equation (5) is used to obtain $\sigma^2_{\eta|\omega}$, which are presented in Figure 11(i) as $\mu_{\eta|\omega} \pm 3 \cdot \sigma_{\eta|\omega}$ and superimposed on the healthy data. A satisfactory fit is obtained with η in Figure 11(i) and therefore it is used further in this section. In Figure 11(ii), the scaled discrepancy measure that is obtained using Equation (8) is presented over the rotational speed. The scaled discrepancy signal, ξ_i, presents the desired property as its magnitude is relatively speed independent.

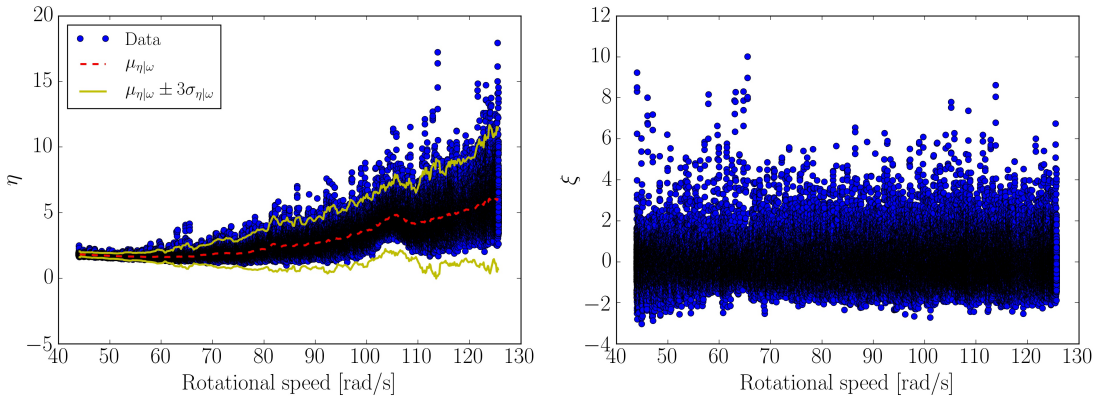

(i) (ii)

Figure 11: The discrepancy data over the rotational speed, originally presented in Figure 5, is presented with the fit $\mu_{\eta|\omega}(\omega)$ and $\sigma_{\eta|\omega}(\omega)$ in Figure 11(i). The processed discrepancy signal is presented in Figure 11(ii) for the healthy data.

The spectrum of the processed discrepancy signal is presented in Figure 12 and it should be highlighted that the amplitude of the BPFO is independent of the rotational speed profile. The slight amplitude differences between the BPFO, estimated under the same operating condition, are attributed to a variation in noise, the random gear component and the model fit which is not perfect as seen in Figure 11. However, a significant improvement has been achieved by processing the discrepancy measure. This makes detecting, localising and trending the bearing damage easier under varying speed conditions.

4. Experimental validation

Two experimental investigations are performed in this section. In the first investigation, the ability of the methodology to detect damage, localise damage and to trend the diagnostic metric over measurement time is investigated. The dataset was acquired under constant operating conditions and therefore the results do not reflect the ability of the methodology to be used under varying speed conditions. Hence, in the second investigation, the ability of the methodology to detect and localise damage is investigated on experimental data that were acquired under varying speed conditions.

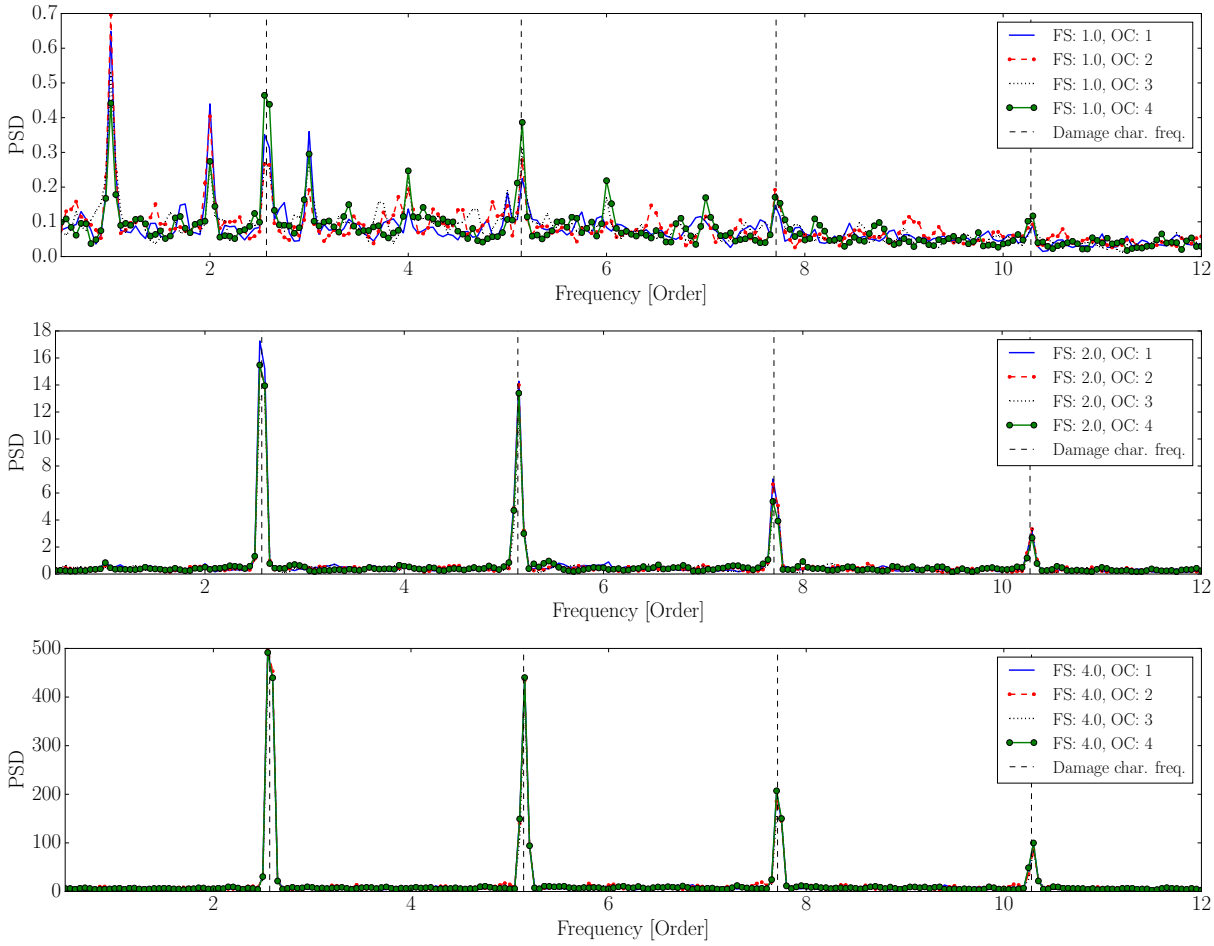

Figure 12: Comparing the spectrum of the processed discrepancy signals for the four operating conditions and the three fault severities that are investigated for the phenomenological gearbox model.

4.1. Investigation 1

The IMS bearing dataset [54, 55] for the case where outer race damage occurred on a bearing, which ultimately resulted in the complete failure of the bearing, is investigated in this section. A schematic of the setup is presented in figure 13. The run-to-failure test-rig contains four bearings supporting the same shaft, where the shaft is connected with a belt to an electric motor. A constant load of 6000 lbs and a constant shaft speed of 2000 rpm were applied during the experiments. Vibration measurements of 1 second long were sampled at 20 kHz, and ultimately 984 measurements were obtained during the experiment until the amount of debris in the oil, that were attached to a magnetic plug, exceeded a predefined level [55].

The proposed methodology was applied to the dataset, where the first ten measure-

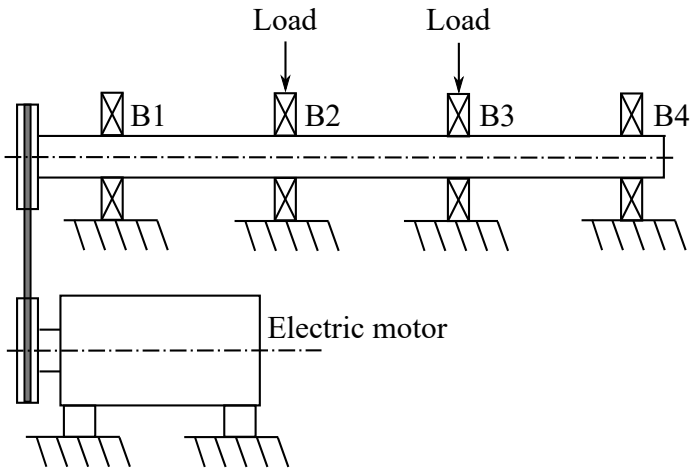

Figure 13: The IMS experimental setup [55]. The different bearings are indicated by B1, B2, B3 and B4. Bearing B1 is the bearing that failed.

ments of bearing B1 that ultimately failed, were used to optimise the Gaussian model. The processed discrepancy signal in the angle domain is used in this section, even though the data were acquired under constant operating conditions. There will not be any benefits from using the proposed discrepancy processing technique in Section 2.5 when the shaft speed is constant, however it is used for consistency. The power spectral density for each measurement was calculated and presented over the measurement number in Figure 14(i), while the spectrum for a single measurement is shown in Figure 14(ii). The theoretical

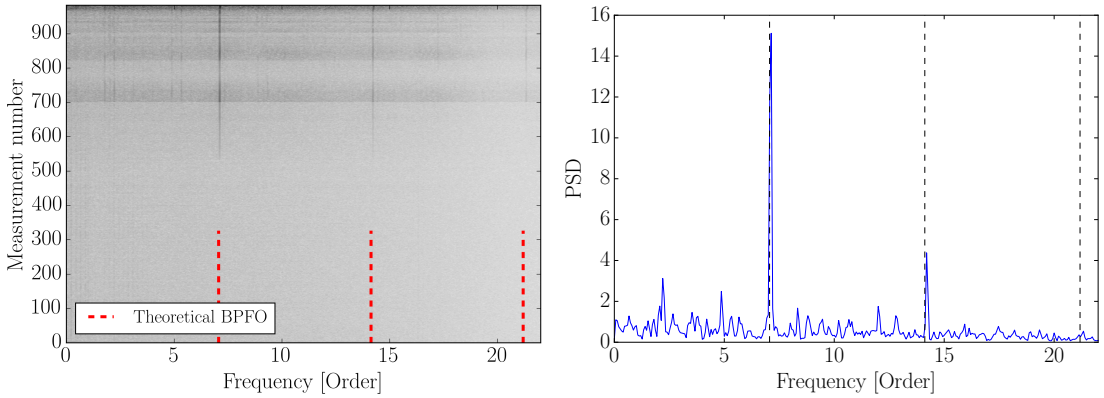

Figure 14: The discrepancy over measurement number and frequency (in shaft orders) is presented for all the measurement files in Figure 14(i), while the spectrum of a single measurement is presented in Figure 14(ii) for the IMS bearing dataset. The theoretical BPFO and its harmonics are presented as vertical, dashed lines in Figure 14(i) and Figure 14(ii).

BPFO component of 7.059 shaft orders and its harmonics are presented in Figure 14 as well. The damage components became visible at the 535th measurement in Figure 14(i).

Lastly, developing and trending a diagnostic metric over the measurement number are investigated. The first proposed metric, is to calculate the Root-Mean-Square (RMS) of the discrepancy signal for each measurement, which is presented over the measurement number in Figure 15. An alarm threshold is considered by calculating the mean μ and

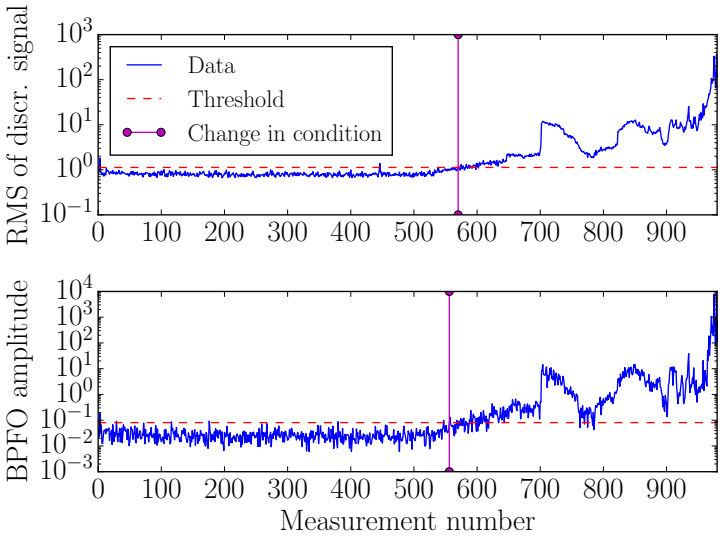

Figure 15: Two diagnostic metrics are shown on a logarithmic scale as function of the measurement number for the IMS dataset. For the first diagnostic metric, the RMS of the entire discrepancy signal is calculated and for the second diagnostic metric the fundamental outer race component in the spectrum for each measurement is calculated.

the standard deviation σ of the diagnostic metric for the first ten measurements, and then calculating $\mu + k\sigma$, where $k = 3$. If the number of measurements used to calculate the alarm threshold is too little, poor estimates of the mean and the standard deviation will be obtained. The second metric that is proposed is the amplitude of the fundamental component of the BPFO. An alarm threshold is calculated with the same method as the RMS metric. The change in condition, estimated at the time instant or measurement number where the mean of three consecutive diagnostic metrics exceed the threshold, is presented in Figure 15. The trending procedure is more robust to false alarms when using three consecutive measurements as opposed to a single measurement.

The diagnostic metrics presented in Figure 15 do not increase monotonically, which

emphasises that the methodology's aim is to infer the presence of damage by detecting the presence of impulses in the signal. The progression of bearing damage, as indicated and discussed by El-Thalji and Jantunen [53], does not result in the magnitude of impulses to increase monotonically, but it can go through increasing and decreasing phases. This possibly reflects the characteristics that are observed in Figure 15.

Hence, from the results in Figure 14 and Figure 15 it is concluded that the developed methodology allows damage to be detected, located and trended prior to the failure of the bearing. The discrepancy signal is sensitive to changes in machine condition and the RMS of the discrepancy signal is a very good metric to be used for fault detection and trending. By using the amplitude of the BPFO component as a metric, the development of localised damage can be detected as well.

4.2. Investigation 2

In this section, four run-up datasets that correspond to four bearing conditions are analysed using the proposed diagnostic methodology. An overview of the setup as well as the data are presented in the next section, whereafter the methodology is applied on the data.

4.2.1. Overview of setup

Experimental data, acquired from a SpectraQuest, Inc. Machinery Fault Simulator, are processed in this section. The experimental setup, presented in Figure 16, consists of a 0.5 HP three-phase electrical motor that has a nominal speed of 3450 rpm and a shaft loader which applies a static load of 49.05 N to the system. The left bearing was in a healthy condition, while the condition of the right bearing, i.e. the testing bearing, was changed between the different experiments. The four bearing conditions that were investigated for the right bearing are presented in Table 1, with the short name that is used in the figures and the analytical defect frequency, calculated from the properties of the bearing, included as well.

For each of the bearing conditions presented in Table 1, a speed run-up was performed

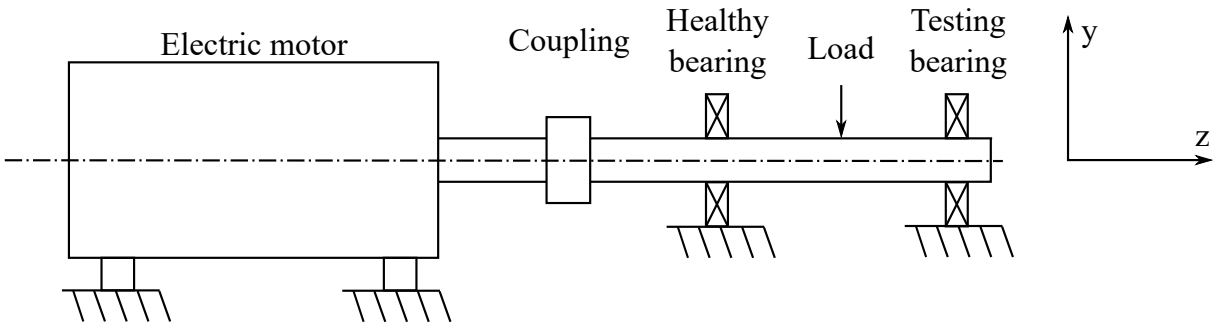

Figure 16: A schematic of the test bench that is investigated for the SpectraQuest, Inc. dataset.

Table 1: Characteristics of the right bearing of the experimental setup in Figure 16.

Testing bearing condition	Short name for measurement	Defect frequency (shaft orders)
Healthy	HH	-
Outer race damage	HO	3.5913
Rolling element damage	HB	2.3751
Inner race damage	HI	5.4087

while various signals such as acceleration measurements and a one-pulse per revolution tachometer signal were acquired. The rotational speed profiles for the four cases, using the tachometer signal information, are presented in Figure 17. The angular acceleration of the

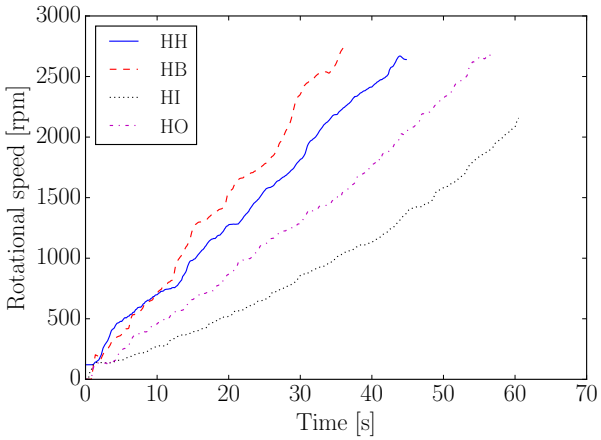

Figure 17: Rotational speeds over measurement time of the four datasets from the SpectraQuest, Inc. setup. The data are labelled as follows: HH: Healthy bearing; HB: Rolling element damage; HI: Inner race damage; HO: Outer race damage.

shaft was different for all four cases, with approximately the same maximum rotational speed obtained in each case. The vibration signals in the y-direction for the four cases listed in Table 1, sampled at 25.6 kHz, are presented in Figure 18. The sensitivity of the

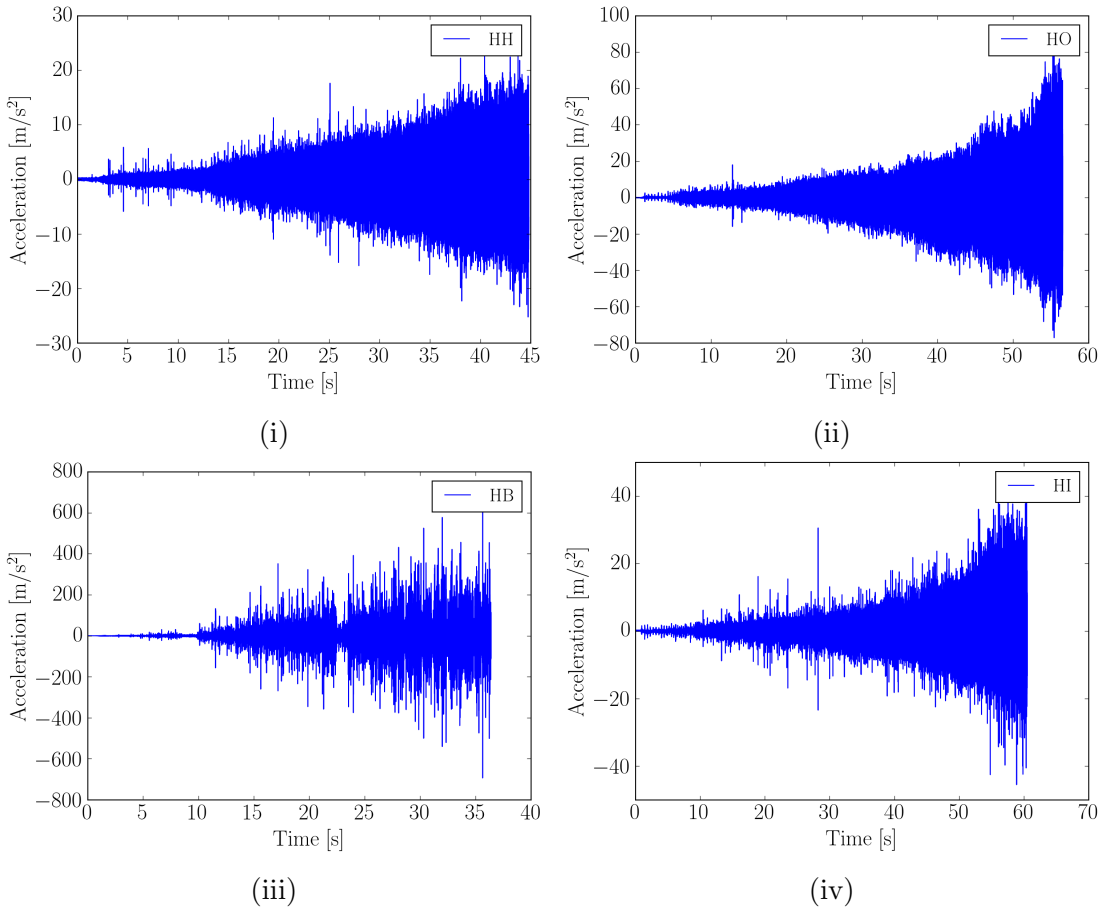

Figure 18: The vibration signals for the healthy testing bearing 18(i) and the testing bearing that has outer race damage 18(ii), rolling element damage 18(iii) and inner race damage 18(iv) are presented.

acceleration signal's amplitude to rotational speed is clearly observed for all four cases in Figure 18.

4.2.2. Results

The proposed feature extraction approach in Section 2.2 was applied to the healthy vibration data, whereafter a model of the features was created following the procedure described in Section 2.3. The discrepancy metric was generated using Equation (3), with the parameters of the aforementioned model, and used with the rotational speed in Figure 17 to estimate $\mu_{\eta|\omega}(\omega)$ and $\sigma_{\eta|\omega}(\omega)^2$ with Equation (4) and (5), respectively. The same feature extraction procedure was applied for the damaged cases, whereafter the discrepancy metric was generated with Equation (3) and processed using Equation (8). The processed discrepancy metric is analysed using Welch's power spectral density estimate

and the results are separately presented for the four bearing conditions in Figure 19. More information on the bearings is given in Table 1.

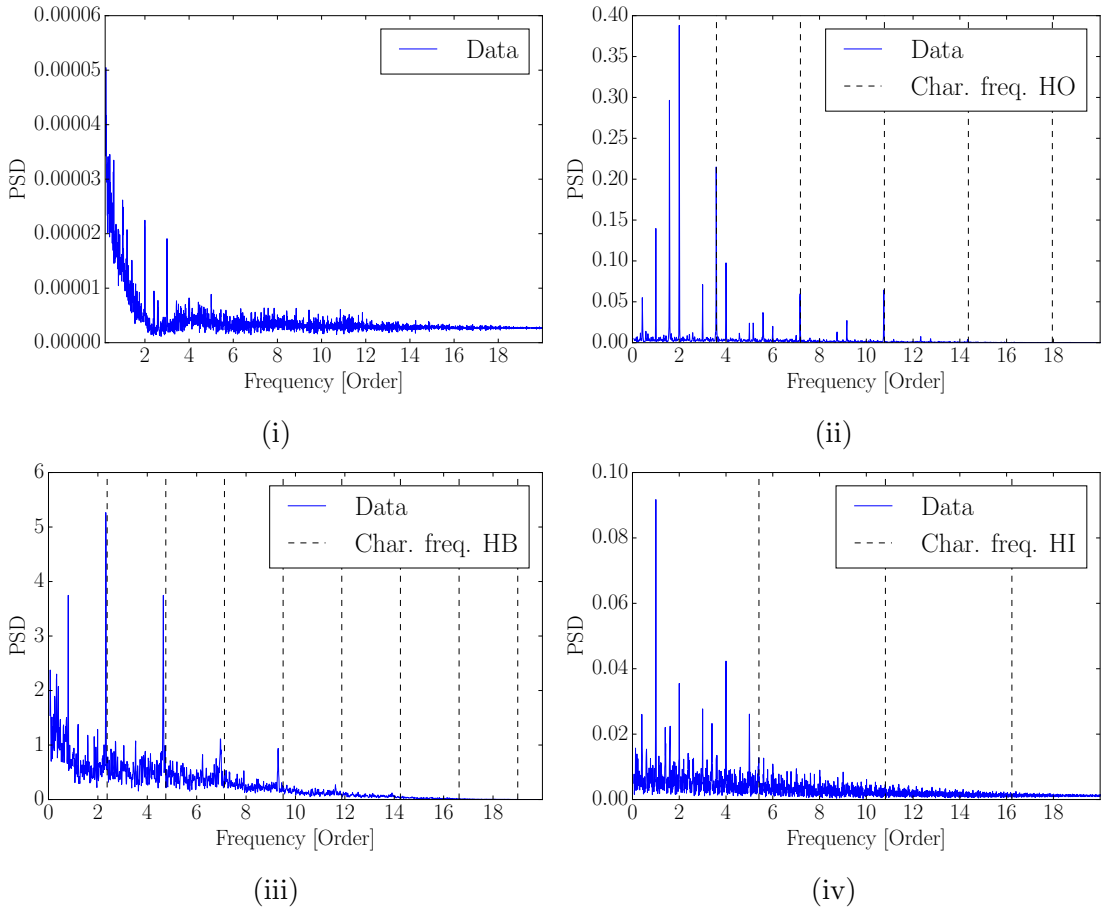

Figure 19: The spectrum of the processed discrepancy signals for the case where the testing bearing was healthy is presented in Figure 19(i) and where it had outer race damage is presented in Figure 19(ii), rolling element damage is presented in Figure 19(iii) and inner race damage is presented in Figure 19(iv).

The spectrum of the healthy bearing in Figure 19(i) contains the expected frequency components such as the shaft orders and its harmonics, but the magnitude of the amplitudes is very small. In the spectrum for the bearing with outer race damage in Figure 19(ii), the fundamental outer race component and its harmonics are seen within the spectrum with other frequency components such as the shaft order and its harmonics. The rolling element damage components dominates the spectrum in Figure 19(iii), with a slight difference between the theoretical defect frequency and the actual defect frequency presented. The inner race component and its harmonics are not clearly seen in the spectrum in Figure 19(iv), because the spectrum is contaminated by other components. The spectrum

of all cases presented in Figure 19 is contaminated by harmonics of the Fundamental Train Frequency (FTF) which is equal to 0.4 shaft orders. The presence of these components can be attributed to an improper installation of the bearing.

The discrepancy data versus the rotational speed data are presented in Figure 20(i) with the fit $\mu_{\eta|\omega}(\omega)$ and $\sigma_{\eta|\omega}(\omega)$ presented as well. The fit in Figure 20(i) does not capture the characteristics of the data properly and this practically indicates that Equation (8) does not scale the data appropriately using the current fit. The discrepancy measure,

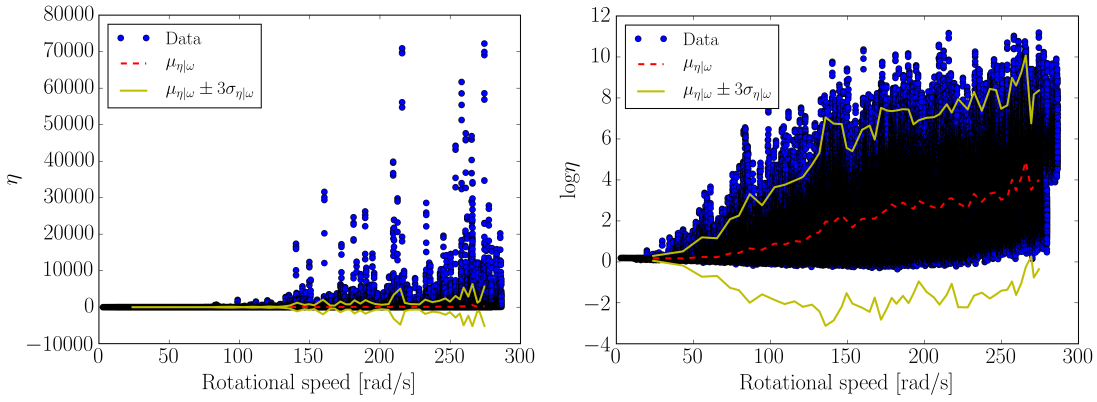

(i) (ii)

Figure 20: The fit of $\mu_{\eta|\omega}(\omega)$ and $\sigma_{\eta|\omega}(\omega)$ is compared in Figure 20(i) for the original discrepancy data η and for $\log\eta$ in Figure 20(ii).

for a fixed rotational speed, is skewed in the direction of increasing discrepancy which means that a Gaussian fit is not appropriate. It is possible to make the distribution more symmetric, by calculating the logarithm of the discrepancy measure i.e. $\log\eta$ instead. Hence, in Equation (4), Equation (5) and Equation (8) the discrepancy measure η is replaced by $\log\eta$ to obtain the result presented in Figure 20(ii). The fit is significantly better when using the logarithm of the data and it can be seen that only the lower bound of the fit (i.e. $\mu - 3\sigma$) deviates from the actual lower bound. The spectrum of the new processed logarithm of the discrepancy signal is presented in Figure 21.

If the spectrum of the healthy bearing in Figure 21(i) is compared to the spectrum of Figure 19(i), it can be observed that the shaft order components are seen more clearly. In Figure 21(ii), the outer race damage components are very prominent in the spectrum. The

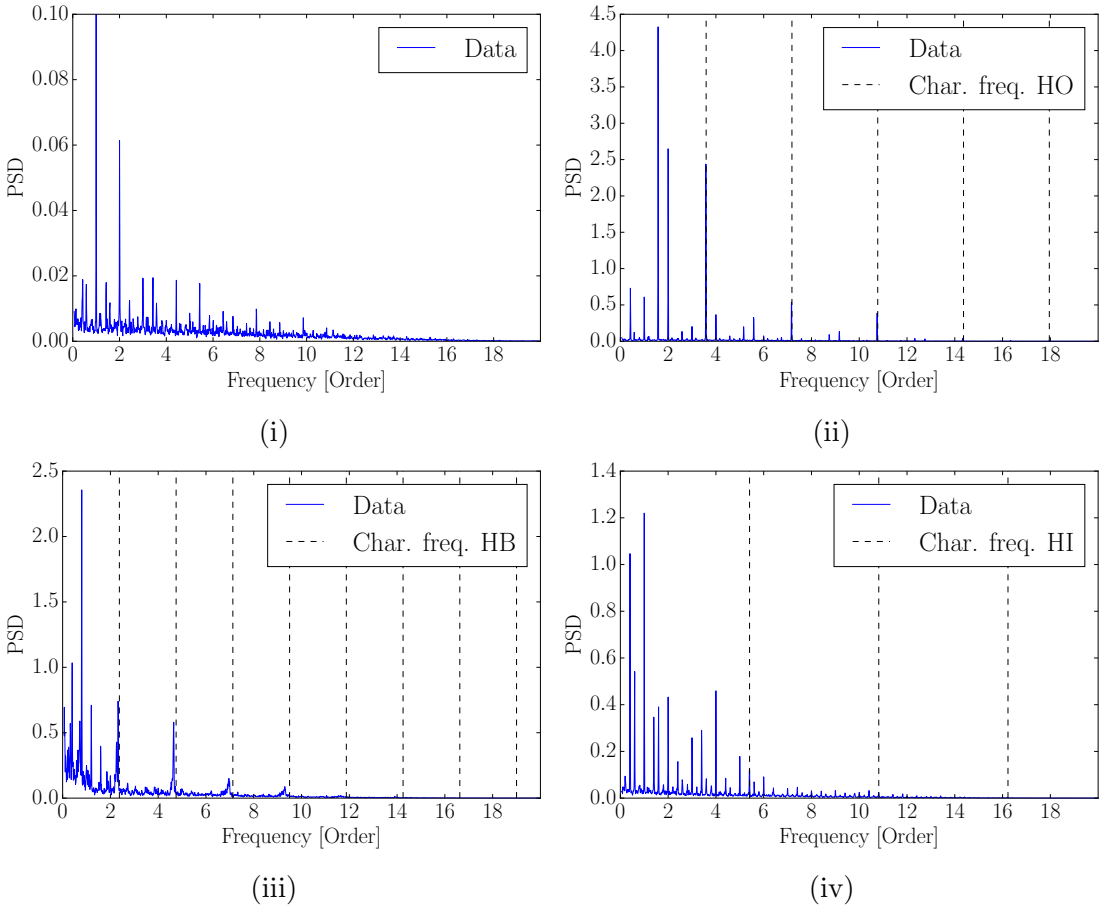

Figure 21: The spectrum of the processed discrepancy signals for the case where the testing bearing was healthy is presented in Figure 21(i) and where it had outer race damage is presented in Figure 21(ii), rolling element damage is presented in Figure 21(iii) and inner race damage is presented in Figure 21(iv).

contaminating frequency components, surrounding the outer race damage components, are smaller with respect to the amplitude of the outer race damage components when compared to the result in Figure 19(ii). The spectrum in Figure 21(iii), contains the rolling element damage component and its harmonics. The rolling element bearing damage components seem slightly smaller with respect to the shaft order components when compared to the spectrum in Figure 19(iii). The improper scaling used in Figure 19(iii) amplified the defect frequencies of the rolling element damage. In the spectrum in Figure 21(iii), it is possible to detect the presence of rolling element damage and the scaling with $\log \eta$ can be consistently used to draw conclusions from future datasets.

The inner race damage components are slightly more prominent in the spectrum in Figure 21(iv) as compared to the spectrum in Figure 19(iv). A zoomed view of the

inner race damage spectrum, presented in Figure 22, indicates that there is an inner race component present and it is surrounded by the shaft order and the other contaminating components.

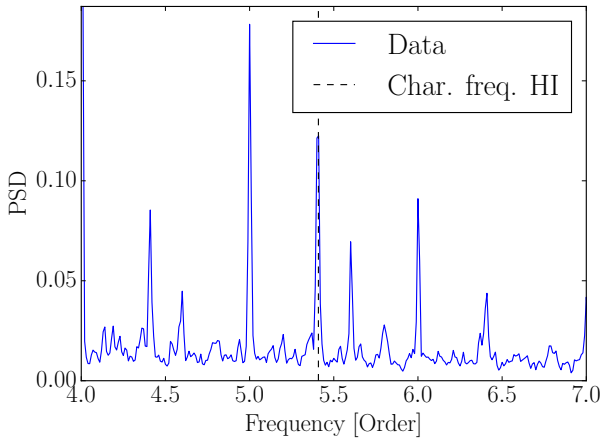

Figure 22: Zoomed view of the spectrum of the inner race damage bearing case (HI) originally presented in Figure 21(iv).

Hence, from the results it is possible to detect the presence of outer race, rolling element and inner race damage components in varying speed conditions using the proposed methodology. Even though the initial results that were obtained by modelling η made it possible to detect the damage components, the results were more robust by using a more appropriate density i.e. when $\log \eta$ was modelled instead. The large speed changes in this dataset complicated the noise distribution of the discrepancy signal due to possible non-linear effects seen in Figure 20. It is therefore suggested that more elaborate noise models need to be investigated for equipment with significant speed changes throughout its operation to ensure that the processed discrepancy signal is speed independent. It is also prevalent from the results that are presented in Figure 21 and Figure 22 that the proposed procedure is not capable of removing the contaminating noise components generated by the 0.4 shaft order components nor the shaft order harmonics. The proposed method is designed to detect the presence of singularities and impulses and therefore the presence of impulses and singularities in the signal will be reflected in the discrepancy signal as well. The contaminating spectral components can be attenuated by methods proposed in literature for example see Refs. [6, 7].

5. Conclusion and recommendations

A bearing diagnostic methodology based on discrepancy analysis is proposed in this paper for variable speed conditions. The bearing diagnostic methodology is combined with a discrepancy post-processing technique which can be utilised for other diagnostic metrics that exhibit speed dependent behaviour. The effectiveness of the methodology has been successfully evaluated using data from a phenomenological gearbox model as well as from two experimental test rigs and it has been demonstrated that the proposed methodology can effectively detect, localise and trend damage in rolling element bearings.

The benefit of the proposed methodology is that the characteristics of the healthy bearing signal are learned, used to generate a discrepancy signal and subsequently the condition of the bearing is inferred under varying speed conditions. This is performed without having historical fault data available and without selecting specific sub-bands in the wavelet packet transform for example, however selecting the most appropriate sub-bands could potentially improve the results. Therefore, the methodology provides a framework which can be used to incorporate existing techniques and new developments in the machine condition monitoring field into the diagnostic process. The discrepancy signal processing technique used in this paper can also be used to make diagnostic metrics more robust.

Future investigations can focus on improving the results with the methodology, by for example incorporating signal processing techniques such as pre-whitening techniques and improving the features that are used. It is also necessary to investigate and compare other feature extraction techniques based on cyclostationary analysis for example. Even though the RMS features of the windowed segments are well motivated and performed well in the investigations, it is necessary to investigate and compare additional features such as the kurtosis to improve the diagnostic capabilities of discrepancy analysis. It is also suggested that different feature models, considered in past gear diagnostics work, need to be compared for bearing diagnostics as well. The diagnostic metrics developed in Section 4.1 are sensitive to changes in machine condition and can therefore potentially serve as an input for a prognostic model as well. It is therefore sensible to investigate

this further in future investigations. Two investigations were performed under variable speed conditions and future investigations can focus on load varying and load and speed varying conditions. Lastly, it is also recommended to critically investigate and validate the methodology on real data acquired from industrial gearboxes found in wind turbines, draglines and air-cooled condenser fans to list a few.

Acknowledgements

The authors gratefully acknowledge the support that was received from the Eskom Power Plant Engineering Institute (EPPEI) in the execution of the research. The authors would also like to acknowledge Siemens Industry Software and Dr. ir. Karl Janssens for allowing the use of the SpectraQuest experimental data. K.C. Gryllias gratefully acknowledges the Research Fund KU Leuven.

Appendix A. Diagnostic processing

In this section, the procedure which is used to estimate the mean and the variance of the conditional distribution $p(\eta|\omega)$ is presented. It is assumed that the actual conditional density of the discrepancy measure η given the rotational speed ω, $p(\eta|\omega)$, is unknown and samples cannot be easily obtained from it. The process is started by considering the analytical form of the expected value $E[\eta|\omega]$

$$E[\eta|\omega] = \int \eta p(\eta|\omega) d\eta. \tag{A.1}$$

If an infinite number of samples is taken from the conditional distribution $p(\eta|\omega)$, then it can be used to calculate the expected value of η given ω

$$E[\eta|\omega] = \lim_{N\to\infty} \frac{1}{N} \sum_{i=1}^{N} \eta_i|\omega, \tag{A.2}$$

where $\eta_i|\omega$ is a sample from $p(\eta|\omega)$. A different form of Equation (A.2) is analysed because it is assumed that it is not possible to sample from $p(\eta|\omega)$ directly

$$E\left[\eta|\omega\right] = \lim_{d\Omega\to 0}\lim_{N\to\infty}\frac{1}{N}\sum_{i=1}^{N}\eta_i|\omega \;\in\; \left[\Omega - d\Omega/2, \Omega + d\Omega/2\right], \tag{A.3}$$

where $\eta_i|\omega$ is a sample from the conditional distribution $p(\eta_i|\omega)$, where the rotational speed $\omega \;\in\; [\Omega - d\Omega/2, \Omega + d\Omega/2]$ and defining the variable Ω in the equation is useful for later. If it is assumed that the actual set of discrepancy measures for a healthy dataset $\{\eta_i\}$ and the corresponding set of rotational speeds $\{\omega_i\}$ are samples from the actual distribution $p(\eta, \omega)$, then it can be used to approximate $E[\eta|\omega]$. Equation (A.3) is extended to accommodate the experimental data

$$E\left[\eta|\omega_j\right] \approx \frac{1}{N_{\eta|\omega}}\sum_{i=1}^{N_{\eta|\omega}}\eta_i|\omega_i \;\in\; \left[\Omega - \Delta\Omega/2, \Omega + \Delta\Omega/2\right], \tag{A.4}$$

with $\omega_j \;\in\; [\Omega - \Delta\Omega/2, \Omega + \Delta\Omega/2]$ and $\eta_i|\omega_i$ denoting the sample η_i for which the corresponding rotational speed ω_i falls within the range $\omega_i \;\in\; [\Omega - \Delta\Omega/2, \Omega + \Delta\Omega/2]$. There are $N_{\eta|\omega}$ samples in the set $\{\omega_i\}$ for which $\omega_i \;\in\; [\Omega - \Delta\Omega/2, \Omega + \Delta\Omega/2]$. Hence, it can be seen from Equation (A.3) that the smaller the window length $\Delta\Omega$ is and the more samples $N_{\eta|\omega}$ are used, the better the approximation in Equation (A.4) becomes. However, because the actual data are considered, there is a compromise between the selected window length and the number of samples that can possibly be used.

Ultimately, this procedure is implemented by generating a grid $\{\Omega_i\}$ of window centres and preselecting the window width $\Delta\Omega$. For each window centre j a single value of $E[\eta|\Omega_j]$ is obtained. Instead of assuming that $E[\eta|\omega]$ is constant for a given window centre and within the bounds, it is assumed that $E[\eta|\omega]$ varies linearly between window centres. Hence, the value of $E[\eta|\omega]$ for a specific ω is obtained by linear interpolation by using the window centres $\{\Omega_i\}$ and the corresponding set $\{E[\eta|\Omega_i]\}$. The notation $\mu_{\eta|\omega}(\omega) = E[\eta|\omega]$ is used in this paper. The approach is easily extended to calculate the variance of the

discrepancy measure given the operating conditions.

Appendix B. Phenomenological gearbox model parameters

The parameters and characteristics of the phenomenological model are presented in this section and are neither based on a specific experimental setup nor a specific gearbox. The natural frequencies of the different components, presented in Table B.2, are unique and in a similar range to Ref. [7].

Table B.2: The parameters in Equation (13) for the various transmission paths.

	$f_{n,i}$ Hz	ζ_i
h_{rg}	3500	0.05
h_{dg}	2000	0.05
h_b	5000	0.05

The fundamental gear mesh component and its nine harmonics' characteristics are presented in Table B.3. Ten components were selected to ensure that the resonance band is properly excited and to ensure that there are many contaminating components. The magnitude of the second and third components are chosen to be the most dominant to replicate phenomena seen in the spectra in Refs. [56, 57].

Table B.3: Values of the parameters used in Equation (14).

i	1	2	3	4	5	6	7	8	9	10
$A_{dg}^{(i)}$	1	1.5	2	1	0.5	0.3	0.2	0.1	0.1	0.05
$\varphi_{dg}^{(i)}$	0	0	0	0	0	0	0	0	0	0

The magnitude of the random gear components in Table B.4 is assumed to have similar characteristics as the spectra in Refs. [56, 57], where the second and third harmonic of the gear mesh frequency are the most dominant in the spectrum.

Table B.4: Values of the parameters used in Equation (15).

i	1	2	3
$A_{rg}^{(i)}$	1	2	3
$\varphi_{dg}^{(i)}$	0	0	0

The coefficients of the linear monotonic functions M_i, used in Equation (14), (15), (17) and (19), are presented in Table B.5.

Table B.5: The parameters that the monotonic function used in Equation (14), (15), (17), and (19). The form of the function is: $M_i(\omega) = a\omega + b$.

	a	b
$M_{dg}(\omega)$	1	0
$M_{rg}(\omega)$	1	0
$M_b(\omega)$	1	0
$M_n(\omega)$	1	0

The standard deviation of the noise σ_n and the random gear component σ_{rg} are presented in Table B.6.

Table B.6: The standard deviation used in Equation (15) and Equation (17).

σ_n	0.1
σ_{rg}	1.0

The F_{const} component used in Equation (19) for the bearing signal is presented in Table B.7. The RMS and the maximum values of the casing signal for a healthy bearing $x_c(t) - x_b(t)$ and for a damaged bearing with different fault severities $x_b(t)$ are compared in Table B.7 as well. The third operating condition profile, presented in Figure 8, is used to obtain the statistics in Table B.7.

Table B.7: The bearing damage characteristics used in Equation (19). The RMS and the maximum are calculated for the third operating condition profile presented in Figure 8.

	FS	F_{const}	RMS	Maximum
$x_c(t) - x_b(t)$	-	-	27.5870200129	159.891754808
$x_b(t)$	1	0.00795774	1.50148614673	31.8616084331
$x_b(t)$	2	0.00795774	2.97797593598	68.710354709
$x_b(t)$	3	0.00795774	6.02045967978	137.575713634

References

[1] C. J. Stander, P. S. Heyns, Instantaneous angular speed monitoring of gearboxes under non-cyclic stationary load conditions, Mechanical Systems and Signal Processing 19 (4) (2005) 817–835.

[2] W. Bartelmus, R. Zimroz, A new feature for monitoring the condition of gearboxes in non-stationary operating conditions, Mechanical Systems and Signal Processing 23 (5) (2009) 1528–1534.

[3] W. Bartelmus, R. Zimroz, Vibration condition monitoring of planetary gearbox under varying external load, Mechanical Systems and Signal Processing 23 (1) (2009) 246–257.

[4] Y. Lin, L. Tu, H. Liu, W. Li, Fault analysis of wind turbines in China, Renewable and Sustainable Energy Reviews 55 (2016) 482–490.

[5] R. B. Randall, J. Antoni, Rolling element bearing diagnostics-A tutorial, Mechanical Systems and Signal Processing 25 (2) (2011) 485–520.

[6] P. Borghesani, P. Pennacchi, R. B. Randall, N. Sawalhi, R. Ricci, Application of cepstrum pre-whitening for the diagnosis of bearing faults under variable speed conditions, Mechanical Systems and Signal Processing 36 (2) (2013) 370–384.

[7] D. Abboud, J. Antoni, S. Sieg-Zieba, M. Eltabach, Envelope analysis of rotating machine vibrations in variable speed conditions: A comprehensive treatment, Mechanical Systems and Signal Processing 84 (2017) 200–226.

[8] J. Antoni, Cyclostationarity by examples, Mechanical Systems and Signal Processing 23 (4) (2009) 987–1036.

[9] J. Urbanek, T. Barszcz, R. Zimroz, J. Antoni, Application of averaged instantaneous power spectrum for diagnostics of machinery operating under non-stationary operational conditions, Measurement 45 (7) (2012) 1782–1791.

[10] R. Zimroz, W. Bartelmus, T. Barszcz, J. Urbanek, Diagnostics of bearings in presence of strong operating conditions non-stationarity - A procedure of load-dependent features processing with application to wind turbine bearings, Mechanical Systems and Signal Processing 46 (1) (2014) 16–27.

[11] J. Dybała, R. Zimroz, Rolling bearing diagnosing method based on Empirical Mode Decomposition of machine vibration signal, Applied Acoustics 77 (2014) 195–203.

[12] J. Singh, A. K. Darpe, S. P. Singh, Bearing damage assessment using Jensen-Rényi Divergence based on EEMD, Mechanical Systems and Signal Processing 87 (2017) 307–339.

[13] C. Mishra, A. K. Samantaray, G. Chakraborty, Rolling element bearing defect diagnosis under variable speed operation through angle synchronous averaging of wavelet de-noised estimate, Mechanical Systems and Signal Processing 72-73 (2016) 206–222.

[14] V. Purushotham, S. Narayanan, S. A.N. Prasad, Multi-fault diagnosis of rolling bearing elements using wavelet analysis and hidden Markov model based fault recognition, NDT & E International 38 (8) (2005) 654–664.

[15] J. Rafiee, M. A. Rafiee, P. W. Tse, Application of mother wavelet functions for automatic gear and bearing fault diagnosis, Expert Systems with Applications 37 (6) (2010) 4568–4579.

[16] K. Gryllias, I. Antoniadis, C. Yiakopoulos, Demodulation of vibration signals generated by defects in rolling element bearings under variable speed using morphological analysis and complex shifted morlet wavelets, in: International Conference Surveillance 9, INSA Euro-Mediterranean, Morocco, May 22-24, 2017.

[17] J. Antoni, R. B. Randall, The spectral kurtosis: Application to the vibratory surveillance and diagnostics of rotating machines, Mechanical Systems and Signal Processing 20 (2) (2006) 308–331.

[18] J. Antoni, Fast computation of the kurtogram for the detection of transient faults, Mechanical Systems and Signal Processing 21 (2007) 108–124.

[19] D. Wang, P. W. Tse, K. L. Tsui, An enhanced Kurtogram method for fault diagnosis

of rolling element bearings, Mechanical Systems and Signal Processing 35 (1-2) (2013) 176–199.

[20] P. W. Tse, D. Wang, The Sparsogram: A new and effective method for extracting bearing fault features, Prognostics and System Health Management Conference (PHM-Shenzhen), 2011 (2011) 1_6.

[21] J. Antoni, The infogram: Entropic evidence of the signature of repetitive transients, Mechanical Systems and Signal Processing 74 (2016) 73–94.

[22] D. Abboud, S. Baudin, J. Antoni, D. Rémond, M. Eltabach, O. Sauvage, The spectral analysis of cyclo-non-stationary signals, Mechanical Systems and Signal Processing 75 (2016) 280–300.

[23] D. Abboud, J. Antoni, Order-frequency analysis of machine signals, Mechanical Systems and Signal Processing 87 (2017) 229–258.

[24] M. Zhao, J. Lin, X. Wang, Y. Lei, J. Cao, A tacho-less order tracking technique for large speed variations, Mechanical Systems and Signal Processing 40 (1) (2013) 76–90.

[25] J. Urbanek, T. Barszcz, J. Antoni, A two-step procedure for estimation of instantaneous rotational speed with large fluctuations, Mechanical Systems and Signal Processing 38 (1) (2013) 96–102.

[26] S. Schmidt, P. S. Heyns, J. P. de Villiers, A tacholess order tracking methodology based on a probabilistic approach to incorporate angular acceleration information into the maxima tracking process, Mechanical Systems and Signal Processing 100 (2018) 630–646.

[27] Q. Leclère, H. André, J. Antoni, A multi-order probabilistic approach for Instantaneous Angular Speed tracking debriefing of the CMMNO'14 diagnosis contest, Mechanical Systems and Signal Processing 81 (2016) 375–386.

[28] B. Samanta, K. R. Al-Balushi, S. Al-Araimi, Artificial neural networks and support vector machines with genetic algorithm for bearing fault detection, Engineering Applications of Artificial Intelligence 16 (78) (2003) 657–665.

[29] K. C. Gryllias, I. A. Antoniadis, A support vector machine approach based on physical model training for rolling element bearing fault detection in industrial environments, Engineering Applications of Artificial Intelligence 25 (2) (2012) 326–344.

[30] D. Fernández-Francos, D. Martínez-Rego, O. Fontenla-Romero, A. Alonso-Betanzos, Automatic bearing fault diagnosis based on one-class ν-SVM, Computers & Industrial Engineering 64 (1) (2013) 357–365.

[31] C. T. Yiakopoulos, K. C. Gryllias, I. A. Antoniadis, Rolling element bearing fault detection in industrial environments based on a K-means clustering approach, Expert Systems with Applications 38 (3) (2011) 2888–2911.

[32] T. Marwala, U. Mahola, F. V. Nelwamondo, Hidden Markov models and Gaussian mixture models for bearing fault detection using fractals, International Joint Conference on Neural Networks, Vancouver, Canada (2006) 3237–3242.

[33] Q. Miao, V. Makis, Condition monitoring and classification of rotating machinery using wavelets and hidden Markov models, Mechanical Systems and Signal Processing 21 (2) (2007) 840–855.

[34] H. Ocak, K. A. Loparo, HMM-based fault detection and diagnosis scheme for rolling element bearings, Journal of Vibration and Acoustics 127 (4) (2005) 299.

[35] T. Heyns, S. J. Godsill, J. P. De Villiers, P. S. Heyns, Statistical gear health analysis which is robust to fluctuating loads and operating speeds, Mechanical Systems and Signal Processing 27 (1) (2012) 651–666.

[36] T. Heyns, P. S. Heyns, R. Zimroz, Combining discrepancy analysis with sensorless signal resampling for condition monitoring of rotating machines under fluctuating

operations, Ninth International Conference on Condition Monitoring and Machinery Failure Prevention Technologies 2 (2) (2012) 52–58.

[37] T. Heyns, P. S. Heyns, J. P. De Villiers, Combining synchronous averaging with a Gaussian mixture model novelty detection scheme for vibration-based condition monitoring of a gearbox, Mechanical Systems and Signal Processing 32 (2012) 200–215.

[38] M. A. F. Pimentel, D. A. Clifton, L. Clifton, L. Tarassenko, A review of novelty detection, Signal Processing 99 (2014) 215–249.

[39] M. Timusk, M. Lipsett, C. K. Mechefske, Fault detection using transient machine signals, Mechanical Systems and Signal Processing 22 (2008) 1724–1749.

[40] M. L. Wong, L. B. Jack, A. K. Nandi, Modified self-organising map for automated novelty detection applied to vibration signal monitoring, Mechanical Systems and Signal Processing 20 (3) (2006) 593–610.

[41] S. Wang, J. Yub, E. Lapirac, J. Lee, A modified support vector data description based novelty detection approach for machinery components, Applied Soft Computing Journal 13 (2) (2013) 1193–1205.

[42] A. Purarjomandlangrudi, A. H. Ghapanchi, M. Esmalifalak, A data mining approach for fault diagnosis: An application of anomaly detection algorithm, Measurement 55 (2014) 343–352.

[43] Y. Pan, J. Chen, L. Guo, Robust bearing performance degradation assessment method based on improved wavelet packet-support vector data description, Mechanical Systems and Signal Processing 23 (3) (2009) 669–681.

[44] G. Georgoulas, T. Loutas, C. D. Stylios, V. Kostopoulos, Bearing fault detection based on hybrid ensemble detector and empirical mode decomposition, Mechanical Systems and Signal Processing 41 (1-2) (2013) 510–525.

[45] P. S. Heyns, R. Vinson, T. Heyns, Rotating machine diagnosis using smart feature selection under non-stationary operating conditions, Insight-Non-Destructive Testing and Condition Monitoring 58 (8) (2016) 1–8.

[46] S. Schmidt, P. S. Heyns, J. P. de Villiers, A novelty detection diagnostic methodology for gearboxes operating under fluctuating operating conditions using probabilistic techniques, Mechanical Systems and Signal Processing 100 (2018) 152–166.

[47] Z. K. Peng, F. L. Chu, Application of the wavelet transform in machine condition monitoring and fault diagnostics: A review with bibliography, Mechanical Systems and Signal Processing 18 (2) (2004) 199–221.

[48] D. H. Diamond, P. S. Heyns, A. J. Oberholster, Online shaft encoder geometry compensation for arbitrary shaft speed profiles using Bayesian regression, Mechanical Systems and Signal Processing 81 (2016) 402–418.

[49] J.-D. Wu, C.-H. Liu, Investigation of engine fault diagnosis using discrete wavelet transform and neural network, Expert Systems with Applications 35 (3) (2008) 1200–1213.

[50] C. M. Bishop, Pattern Recognition and Machine Learning, Springer, 2006.

[51] P. W. Goldberg, C. K. I. Williams, C. M. Bishop, Regression with input-dependent noise: A Gaussian process treatment, Advances in Neural Information Processing Systems 10 (1997) 493–499.

[52] C. M. Bishop, C. S. Qazaz, Regression with input-dependent noise: A Bayesian treatment, Advances in Neural Information Processing Systems 9 9 (1991) (1997) 347–353.

[53] I. El-Thalji, E. Jantunen, A summary of fault modelling and predictive health monitoring of rolling element bearings, Mechanical Systems and Signal Processing 60-61 (2015) 252–272.

[54] J. Lee, H. Qiu, J. Yu, Rexnord Technical Services, IMS, University of Cincinnati. "Bearing Data Set", NASA Ames Prognostics Data.
URL https://ti.arc.nasa.gov/c/3/

[55] H. Qiu, J. Lee, J. Lin, G. Yu, Wavelet filter-based weak signature detection method and its application on rolling element bearing prognostics, Journal of Sound and Vibration 289 (2006) 1066–1090.

[56] W. Bartelmus, F. Chaari, R. Zimroz, M. Haddar, Modelling of gearbox dynamics under time-varying nonstationary load for distributed fault detection and diagnosis, European Journal of Mechanics, A/Solids 29 (4) (2010) 637–646.

[57] P. D. McFadden, Low frequency vibration generated by gear tooth impacts, NDT International 18 (5) (1985) 279–282.